Model of Performance of a Regenerative Hydrogen Chlorine Fuel Cell for Grid-Scale Electrical Energy Storage

Jason Rugolo, Brian Huskinson, Michael J. Aziz [†]

Harvard School of Engineering and Applied Sciences, Cambridge, MA 02138, USA

[†]Corresponding Author. maziz@harvard.edu. phone: +1 (617) 495-9884. fax: +1 (617) 495-9837.

We develop a model for a regenerative hydrogen-chlorine fuel cell (rHCFC) including four voltage loss mechanisms: hydrogen electrode activation, chlorine electrode activation, chlorine electrode mass transport, and ohmic loss through the membrane. The dependences of each of these losses as a function of two "operating parameters", acid concentration and temperature; and five "engineering parameters", exchange current densities at both electrodes, membrane thickness, acid diffusion layer thickness, and cell pressure, are explored. By examining this large parameter space, we predict the design target and ultimate limitations to the performance characteristics of this cell. We identify chlorine electrode activation as the dominant contribution to the loss for low current density, high-efficiency operation and membrane resistance as the dominant contribution to the loss at maximum galvanic power density. We conclude that, with further research, a more optimal cell could be developed that operates at greater than 90% voltage efficiency at current densities $>1 \frac{\text{A}}{\text{cm}^2}$ in both electrolytic and galvanic modes.

Introduction

Inexpensive and efficient electricity storage devices are in growing demand to solve problems associated with managing the modern electrical grid (1). Of particular interest are high energy capacity devices suited for balancing the intermittent nature of wind and solar photovoltaic power production. With most energy storage systems, such as conventional battery technologies, both the power and energy components of the system scale together.

1

If an application requires either more power or more energy, one must buy both more power *and* more energy. For this reason, it is exceedingly difficult for these types of systems to scale to grid-level storage. In contrast, flow batteries and regenerative fuel cells maintain a modular separation between the power elements of the system (the cell stack) and the energy elements of the system (the reactant and product storage tanks). This permits independent scaling of the two.

An essential characteristic of any electricity storage technology is its round-trip efficiency. Energy is lost both during charging and discharging, making the cell efficiency particularly important, because the efficiency is approximately squared for the round-trip. The benefit of developing a regenerative hydrogen-chlorine fuel cell (as opposed to a regenerative fuel cell of another type, e.g. hydrogen-oxygen) lies in the relatively fast kinetics at the chlorine electrode. Fundamentally, this occurs because the chloride oxidation reaction is a one-electron process. Fast kinetics allow for very high round-trip efficiencies, and electrode kinetics arguably present the largest technological barrier to the implementation of any specific fuel cell chemistry.

The regenerative hydrogen-chlorine fuel cell (rHCFC) is an electrical energy storage device that facilitates the electrochemical reaction $H_2(g) + Cl_2(g) \rightleftharpoons 2HCl(aq)$. In discharge (galvanic) mode, H_2 and Cl_2 react to produce electricity and HCl(aq). In charge (electrolytic) mode, electricity is consumed to split HCl(aq) into H_2 and Cl_2, which is then stored in tanks until the electricity is needed (Figure 1). Compared to most flow batteries, the energy density of the rHCFC can be higher, and the reactants involved are abundant and inexpensive. Also, it is important to note that there is no solid electrode or storage medium involved in a change of state, which can lead to dimensional instability (e.g. dendrite growth) and rapid cycle fatigue.

Much of the early research on rHCFCs focused on high-power applications of these cells, often when cost was not of paramount importance. They were studied for use in the MX missile defense program in the early 1980s (2), and rHCFC studies for space power applications were also of interest to NASA (3). In both cases, the high cell potential and corresponding high energy density of the rHCFC were the important cell characteristics motivating this research. During the energy crises of the 1970s, rHCFC storage systems were also studied for general electricity storage applications such as utility-scale grid storage and solar balancing (4-6). In the latter reference, power densities in excess of 300 $\frac{\mathrm{mW}}{\mathrm{cm}^2}$ were achieved. The studies provided proof of concept and were promising, but, as energy costs stabilized in the 1980s, interest in energy technologies declined in general, and rHCFC studies, mostly carried out in industry, were discontinued.

Because fuel cell materials and systems have undergone vast improvements in the intervening years, rHCFCs have potential today as viable grid-scale electrical energy storage systems. Indeed, more recent experimental studies have led to improved cell performance, with power densities now beyond 500 $\frac{\mathrm{mW}}{\mathrm{cm}^2}$ (7). This paper presents a simplified rHCFC model that is intended to provide insight into the relative magnitudes of the cell losses and therefore to guide rHCFC research and development. To our knowledge, there is no extant model in the literature that explores such a large parameter space, particularly in the context of high efficiency operation. Different approaches to modeling this or related types of systems can be found in the literature (4,8,9). Although we do not attempt to
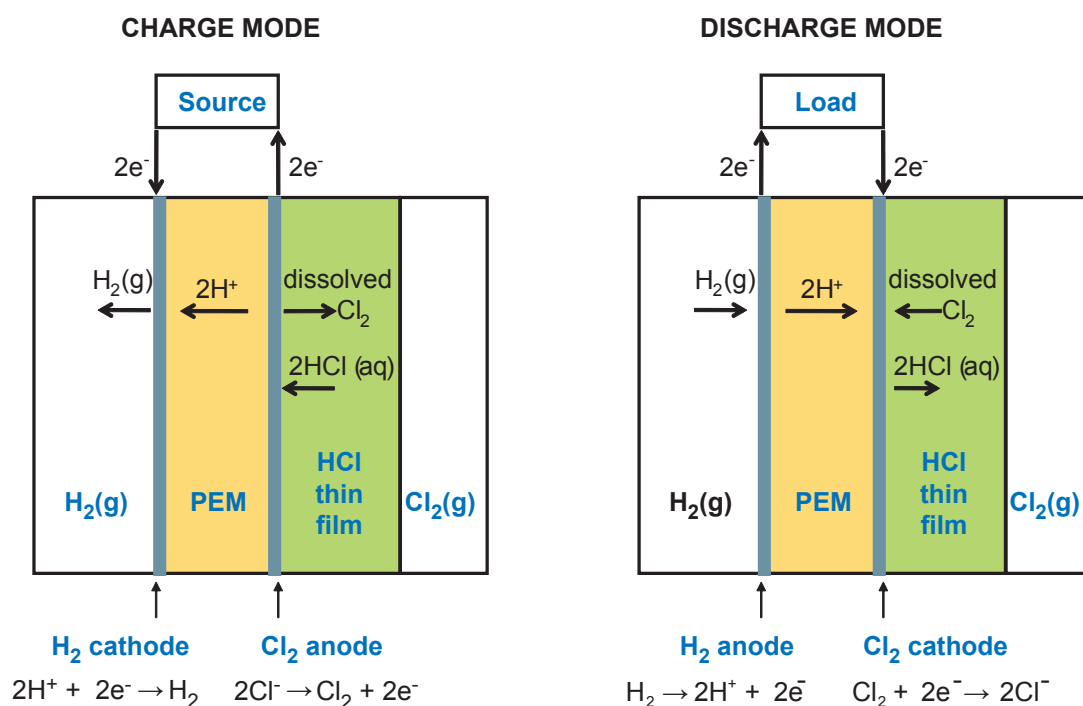
CHARGE MODE

| Source |

$2e^-$ ↓ ↑ $2e^-$

$H_2(g)$ ← $2H^+$ ←   dissolved →Cl_2

2HCl (aq) ←

$H_2(g)$ PEM   HCl thin film $Cl_2(g)$

↑ ↑

H_2 cathode   **Cl_2 anode**

$2H^+ + 2e^- \rightarrow H_2$ $2Cl^- \rightarrow Cl_2 + 2e^-$

DISCHARGE MODE

| Load |

$2e^-$ ↑ ↓ $2e^-$

$H_2(g)$ → $2H^+$ →   dissolved ←Cl_2

2HCl (aq) →

$H_2(g)$ PEM   HCl thin film $Cl_2(g)$

↑ ↑

H_2 anode   **Cl_2 cathode**

$H_2 \rightarrow 2H^+ + 2\bar{e}$ $Cl_2 + 2\bar{e} \rightarrow 2Cl^-$

Figure 1: rHCFC schematic. In charge or electrolytic mode, hydrochloric acid is electrolyzed to produce hydrogen and chlorine using electrical energy from an external source. The products are stored in tanks for future re-conversion to electricity. In discharge or galvanic mode, hydrogen and chlorine react to produce hydrochloric acid and electricity.

predict operating cell potentials with the degree of precision that might be possible with a more complex and detailed model, the simplifications permit a broad survey of a large and complicated parameter space which otherwise could not be explored.

The simplified one-dimensional cell design under consideration is shown in Figure 1. The model focuses on four voltage losses within the cell: hydrogen electrode activation, proton-exchange membrane (PEM) ohmic loss, chlorine electrode activation, and chlorine electrode mass transport. Each loss is modeled a function of current density. We vary the cell's operating parameters (OPs: temperature and acid concentration) for a given set of engineering parameters (EPs: exchange current densities, reservoir pressure, PEM thickness, acid diffusion layer thickness) in order to find the best performance over a range of operating conditions. We then systematically vary the EPs and discuss the effects on the resulting cell performance. The primary metric used to gauge cell performance in this model will be the cell power density at 90% galvanic efficiency.

The chlorine electrode is assumed to be smooth, without a porous gas diffusion layer (GDL), in order to simplify the mass transport model. In a real cell, it would likely be impractical to omit a GDL because the PEM requires support and the lateral conductivity

of a fuel cell electrode is typically unacceptably low. Furthermore, a GDL is responsible for evenly transporting reactants from the flow channels to the catalyst layers. In principle, it is possible to achieve support by constantly maintaining a chlorine overpressure and to achieve lateral conductivity by embedding small cross-section conductors in the electrode, but these methods are unlikely to be implemented due to unnecessary complication and cost. In this model, we intend the mass transport modeling to represent a statistically-averaged behavior, understanding that the local real loss behavior on a complicated three-dimensional, porous electrode could lie to one side or the other of the mean mass transport loss computed here. We expect the conclusion of the model – that losses due to mass transport limitations are insignificant compared to other losses when the cell is operated at low current density for high efficiency – to be unchanged by future work involving three-dimensional mass transport.

The model was used to evaluate cell potentials in both charge mode and discharge mode. For the majority of results presented in this paper, we omit the electrolytic, charge-mode behavior. Typically, a cell that shows good performance in discharge mode also shows good performance in charge mode (particularly within the confined concentration range used in this model), allowing us to simplify the presentation of the model results.

Symbols

a_{Cl_2}	activity of chlorine gas
a_{H_2}	activity of hydrogen gas
$a_{HCl(aq)}$	activity of hydrochloric acid
Ca	capillary number
C_O^{bulk}	bulk concentration of oxidized form (Cl_2), $\frac{mol}{cm^3}$
C_O^S	concentration of oxidized form (Cl_2) near the electrode surface, $\frac{mol}{cm^3}$
C_R^{bulk}	bulk concentration of reduced form (Cl^-), $\frac{mol}{cm^3}$
C_R^S	concentration of reduced form (Cl^-) near the electrode surface, $\frac{mol}{cm^3}$
C_{sat}	saturated concentration of Cl_2 in HCl(aq), $\frac{mol}{cm^3}$
D	diffusion coefficient, $\frac{cm^2}{s}$
D_{Cl^-}	diffusion coefficient of Cl^- in HCl(aq), $\frac{cm^2}{s}$
D_{Cl_2}	diffusion coefficient of Cl_2 in HCl(aq), $\frac{cm^2}{s}$
E	cell potential, V
E_0'	standard cell potential, V
E_{eq}	equilibrium potential, V
f	simplifying parameter in Nernst equation, V^{-1}
H	Henry's law coefficient, $\frac{g}{L \cdot atm}$
h_1	$a_{HCl(aq)}$ fit, 0.33866-0.001283T
i	cell current density, $\frac{mA}{cm^2}$
i_0^{Cl}	chlorine exchange current density, $\frac{mA}{cm^2}$
i_0^H	hydrogen exchange current density, $\frac{mA}{cm^2}$
i_L	cell limiting current density, $\frac{mA}{cm^2}$
J	diffusive flux of species, $\frac{mol}{cm^2 \cdot s}$
l	proton-exchange membrane thickness, cm
m	molality, $\frac{mol}{kg}$
M	molarity, $\frac{mol}{L}$
p	cell power density, $\frac{mW}{cm^2}$
p_{Cl_2}	chlorine gas partial pressure, atm
p_{H_2}	hydrogen gas partial pressure, atm
T	temperature, degrees Celsius
V_b	bubble velocity, $\frac{m}{s}$
w	capillary channel width, cm

Greek letters

α	transfer coefficient
α'	parameter in Henry's law coefficient fit, grams-chlorine per liter/grams-HCl per liter · atm
β	parameter in Henry's law coefficient fit, grams-chlorine per liter/atm
γ_m	activity coefficient of HCl(aq)
ε	HCl(aq) thin film thickness, cm
η	cell efficiency
η_{Cl}	total chlorine electrode activation overpotential (including mass transport effects), V
η_{Cl}'	concentration-independent chlorine electrode activation over-

A_ρ	ρ_{HCl} fit, 20.46
A_ϕ	$a_{HCl(aq)}$ fit, $0.39205 \frac{mol^{-1/2}}{kg^{-1/2}}$
a_1	membrane conductivity fit, -0.0178
a_2	membrane conductivity fit, 0.000389
B_ρ	ρ_{HCl} fit, -0.09435
B	$a_{HCl(aq)}$ fit, $1.4 \frac{mol}{kg}^{-1/2}$
b_1	membrane conductivity fit, 0.891
b_2	membrane conductivity fit, 0.00398
$b_{2,\gamma}$	$a_{HCl(aq)}$ fit, 0.006
$b_{3,\gamma}$	$a_{HCl(aq)}$ fit, -9.7×10^{-5}
C_ρ	ρ_{HCl} fit, 0.00109
c_1	membrane conductivity fit, 2.58
c_2	membrane conductivity fit, 2.55
D_ρ	ρ_{HCl} fit, -1.227
d_1	membrane conductivity fit, 4.20
d_2	membrane conductivity fit, 2.23
E_ρ	ρ_{HCl} fit, 0.01269
F	Faraday's constant, $96485 \frac{C}{mol}$
F_ρ	ρ_{HCl} fit, -0.000198
k_B	Boltzmann's constant, $8.617 \times 10^{-5} \frac{eV}{K}$
M_{Cl_2}	molecular weight of Cl_2, $70.9 \frac{g}{mol}$
M_{H_2O}	molecular weight of H_2O, $0.0180 \frac{kg}{mol}$
M_{HCl}	molecular weight of HCl, $36.461 \frac{g}{mol}$
m_0	reference molality, $1 \frac{mol}{kg}$
p_0	standard pressure, 1 atm
R	ideal gas constant, $8.314 \frac{J}{mol \cdot K}$

The Model

The purpose of this model is to determine the cell potential, in volts, as a function of current density, in $\frac{mA}{cm^2}$, for a given set of OPs and EPs. In this study, we consider the EPs and OPs as well as the dependent physical properties that determine cell losses, such as PEM conductivity and chlorine solubility and diffusivity in HCl(aq). Our objectives are to predict cell efficiency and cell power density p as functions of current density and to determine how these functions change as we vary both the OPs and the EPs.

The operating efficiency of the cell is a piecewise function of current density i, with one expression for the galvanic direction and a different one for the electrolytic direction. In the galvanic case (which we take as defining positive i), hydrogen and chlorine react to produce hydrochloric acid and electricity. The efficiency is the electrical energy per charge produced (the cell potential $E(i)$), divided by the electrical energy per charge that could be produced reversibly (the equilibrium potential E_{eq}). In the electrolytic case (negative i), electrical energy is supplied to split HCl(aq) into H_2 and Cl_2 for energy storage. Here, the efficiency is the maximum possible electrical energy per charge stored, E_{eq}, divided by

the electrical energy per charge spent in doing the electrolysis, $E(i)$:

$$\text{cell efficiency} = \begin{cases} 1 & : i = 0; \\ \frac{E(i)}{E_{eq}} & : i > 0; \\ \frac{E_{eq}}{E(i)} & : i < 0. \end{cases} \quad [1]$$

The power density, in $\frac{\text{mW}}{\text{cm}^2}$, is the amount of power produced per cell area. It is equal to the cell potential multiplied by the current density:

$$p = i \cdot E(i). \quad [2]$$

Because of the high cost of fuel cells per unit cell area, cells having high efficiencies at large power densities are desirable.

The cell potential deviates from its equilibrium value due to several loss mechanisms, all of which lead to the generation of heat in the cell. We identify four overpotentials in the cell: the hydrogen and chlorine electrode overpotentials (η_H and η_{Cl}; the latter actually includes two losses: one due to electrode activation and one due to mass transport limitations at the chlorine electrode), and the membrane resistance overpotential (η_R). Each overpotential is a function of current density and depends on the OPs and a subset of the EPs.

The overall cell potential can thus be expressed as the equilibrium cell potential minus the individual losses:

$$E(i) = E_{eq} - \eta_R(i) - \eta_H(i) - \eta_{Cl}(i), \quad [3]$$

where all of the above quantities are in volts.

E_{eq} is a function of temperature and of the activities of the reactants and products, which themselves depend on temperature, pressure, and concentration. η_R is determined by the conductance of the membrane, which depends on temperature, acid concentration, and membrane thickness. The overpotentials at the two electrodes arise from two different effects: an activation loss due to the kinetics involved with the electron transfer at the surface, and a mass transport loss due to the depletion of the reactants and enrichment of the products near the electrode surface at non-zero current densities. We ignore the mass transport effect at the hydrogen electrode due to presumed fast transport of gaseous hydrogen, whereas we include the chlorine mass transport because of the relatively slow transport of Cl_2 (aq) in aqueous solution.

The equilibrium potential, E_{eq}

The equilibrium potential is that of the combined half-cell reactions, where all potentials are relative to that of a standard hydrogen electrode (SHE):

$$H_2(g) \rightleftharpoons 2H^+(aq) + 2e^- \qquad E_{eq} = 0.000 \text{ V}; \quad [4a]$$

$$Cl_2(aq) + 2e^- \rightleftharpoons 2Cl^-(aq) \qquad E_{eq} = 1.358 \text{ V}. \quad [4b]$$

The equilibrium potential can be described by the Nernst equation:

$$E_{eq} = E_0' + \frac{1}{2f} \ln \left(\frac{a_{Cl_2} a_{H_2}}{a_{HCl(aq)}^2} \right), \qquad [5]$$

where $f = F/(R(T+273.15))$ [V^{-1}], $R = 8.314 \frac{J}{mol \cdot K}$ is the universal gas constant, $F = 96485 \frac{C}{mol}$ is Faraday's constant, and T is the temperature in degrees Celsius. The activities of Cl_2 and H_2 are denoted a_{Cl_2} and a_{H_2}, respectively.

E_0' is the temperature-dependent equilibrium potential when all activities are unity. E_0' must be chosen so that $E_{eq} = 1.358$ V at the standard temperature, pressure, and concentration of 25 °C, 1 atm, and 1 M, respectively (10). Assuming the difference between reactant and product entropies is independent of temperature, E_0' is a linear function of temperature, whose slope is given by the entropy of formation divided by $2f$:

$$E_0' = 1.7364 - 0.00126(T + 273.15). \qquad [6]$$

$a_{HCl(aq)}$ is the mean ionic activity of aqueous hydrochloric acid, which depends on T and the concentrations of the ionic species. For dilute or ideal solutions, the activity is directly proportional to the concentration according to Henry's law. For non-ideal concentrated solutions, however, the activity coefficient can vary significantly, and the activity deviates from Henry's law behavior. In the model, we define the activity in the following way:

$$a_{HCl(aq)} = \gamma_m \frac{m}{m_0}, \qquad [7]$$

where γ_m is the unitless activity coefficient, which depends on temperature and concentration, m is the molality in $\frac{mol}{kg \ solvent}$, and m_0 is the reference molality of 1 $\frac{mol}{kg}$. Partanen *et al.* have studied in depth the concentration and temperature dependence of the activity of hydrochloric acid (11). They present an "extended" Hückel equation that approximates the activity to a precision corresponding to 3 mV in the equilibrium potential over the molality range of 0 to 16 $\frac{mol}{kg}$, and a temperature range of 0 to 50 °C. γ_m is presented as a function of the solution molality, m, and temperature, T in Celsius (Eq. 12 in ref. 11):

$$\ln \gamma_m = \frac{-3A_\phi \sqrt{m}}{1 + B\sqrt{m}} + h_1 \left(\frac{m}{m_0} \right) + b_{2,\gamma} \left(\frac{m}{m_0} \right)^2 + b_{3,\gamma} \left(\frac{m}{m_0} \right)^{7/2} - \ln(1 + 2M_{H_2O}m), \quad [8]$$

where $M_{H_2O} = 0.0180 \frac{kg}{mol}$ is the molecular weight of water, $A_\phi = 0.39205$ (mol$\cdot$kg^{-1})$^{-1/2}$, $B = 1.4$(mol$\cdot$kg^{-1})$^{-1/2}$, $h_1 = 0.33866 - 0.001283T$, $b_{2,\gamma} = 0.006$, and $b_{3,\gamma} = -9.7 \times 10^{-5}$, where the latter three are unitless.

To convert molality to molarity, $M \left[\frac{mol \ solute}{L \ solution} \right]$, we use the following expression:

$$m = \frac{1000M}{\rho_{HCl(aq)} - M_{HCl}M} \qquad [9]$$

where $M_{HCl} = 36.461 \frac{g}{mol}$ is the molecular weight of HCl, and $\rho_{HCl(aq)} \left[\frac{kg}{m^3} \right]$ is the density of the acid solution. The density itself is a function of temperature and concentration, and

has been presented in empirical form by Novotný and Söhnel (12):

$$\rho_{HCl(aq)} = \rho_{H_2O} + A_\rho M + B_\rho MT + C_\rho MT^2 + D_\rho M^{3/2} + E_\rho M^{3/2}T + F_\rho M^{3/2}T^2, \quad [10]$$

where the temperature-dependent density of water, $\rho_{H_2O} \left[\frac{kg}{m^3}\right]$, is given by the empirical expression:

$$\rho_{H_2O} = 999.65 + 0.20438T - 0.06174T^{3/2}. \quad [11]$$

The parameters are as follows: $A_\rho = 20.46$, $B_\rho = -0.09435$, $C_\rho = 0.00109$, $D_\rho = -1.227$, $E_\rho = 0.01269$, and $F_\rho = -0.000198$, each having units necessary to give their respective terms density units of $\frac{kg}{m^3}$. Substituting Equations 8, 9, and 10 into Equation 7 yields a precise temperature- and molarity-dependent hydrochloric acid activity.

We treat both H_2 and Cl_2 as ideal gases, resulting in a combined error in E_{eq} of less than 1 mV, whose activities are given by:

$$a_{H_2} = \frac{p_{H_2}}{p_0}, \quad [12]$$

and

$$a_{Cl_2} = \frac{p_{Cl_2}}{p_0}, \quad [13]$$

where p_0 is the standard pressure of 1 atm.

Figure 2 shows E_{eq} as a function of temperature for several different activity cases. The curve labeled "Standard" refers to the case with the chlorine and hydrogen pressures set to 1 atm and the HCl(aq) concentration set to 1 M. At 25 °C on the standard curve, the standard chlorine reversible potential of 1.358 V is observed. The envelope bounded by the high and low curves is the space of equilibrium potentials explored in this study. Given due consideration to the range of applicability of each component of the model, we will only study the temperature range 5-75 °C, the molarity range 0.5-6 M, and the pressure range 1-5 atm. The curve labeled "High" is the case in which a_{Cl_2} and a_{H_2} are their highest ($p_{Cl_2} = p_{H_2} = 5$ atm), and $a_{HCl(aq)}$ is its lowest (at a molarity of 0.5 M), yielding the highest equilibrium potentials as a function of temperature explored with this model. The curve labeled "Low" is the opposite extreme case, in which the gas activities are their lowest (1 atm), and the acid activity the highest (6 M), such that the lowest potentials are observed.

The membrane resistance overpotential, η_R

The resistive overpotential due to ohmic drop across the membrane takes the following form:

$$\eta_R = \frac{l}{\sigma} \frac{i}{1000}, \quad [14]$$

where l [cm] is the membrane thickness, $\sigma \left[\frac{1}{\Omega \cdot cm}\right]$ is the membrane conductivity, $i \left[\frac{mA}{cm^2}\right]$ is the current density, and η_R is the resistive overpotential in volts (the factor of 1000 assures consistency in units). Commercial DuPont Nafion membranes are typically available in thicknesses ranging from 25 to 250 μm. From a voltage loss perspective, it always helps to
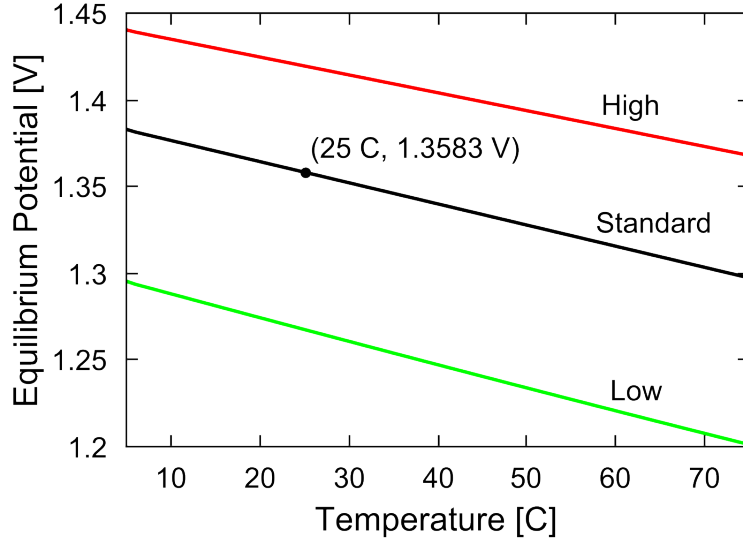
Figure 2: Range of equilibrium potentials explored in this study. The two curves marked "High" and "Low" define the envelope. The "Standard" curve is E_{eq} for 1 M solution and 1 atm gases. The "High" curve is for 0.5 M solution and 5 atm gases. The "Low" curve is for 6 M solution and 1 atm gases.

decrease the thickness of the membrane, though this can only be done to a certain extent in practice: mechanical integrity of the membrane is very important, as membrane rupture would allow the uncontrolled mixing and reaction of H_2 and Cl_2 gases. Furthermore, reactant crossover will increase with the use of thinner membranes, lowering the current efficiency of the cell. Thus, the membrane thickness is also practically limited by the degree of reactant crossover that can be tolerated in a given system. Yeo and McBreen (13) measured the extent of chlorine crossover in a hydrogen-chlorine system using a Nafion 120 membrane (250 μm thick), and, in a 15% HCl solution saturated with Cl_2 gas at 25 °C, the crossover current was measured to be 0.2 $\frac{mA}{cm^2}$. Assuming the crossover current is inversely proportional to membrane thickness, losses on the order of 2 $\frac{mA}{cm^2}$ could reasonably be expected for a 25 μm membrane, the thinnest membrane considered in this study. Thus, chlorine crossover should contribute a loss of less than 1% for the vast majority of cell operational regimes. Hydrogen crossover can occur as well, but, because of the very low solubility of H_2 gas in the HCl electrolyte, the extent of crossover will be less than that of Cl_2 gas (the crossover current is a function of the product of the reactant diffusivity and the reactant solubility). In another study, measured hydrogen crossover currents were observed to be about 60% of the value of the chlorine crossover currents (9).

We use the data of Yeo and McBreen (13) for the conductivity of Nafion 120 as a function of temperature and HCl(aq) concentration, and assume that the conductivity is independent of membrane thickness. Our empirical fit is given by the following:

$$\sigma = \left(a_1 + \frac{b_1}{(M-c_1)^2 + d_1^2} \right) + \left(a_2 + \frac{b_2}{(M-c_2)^2 + d_2^2} \right) T, \qquad [15]$$

10

where the fitting parameters have these values: $a_1 = -0.0178$, $b_1 = 0.891$, $c_1 = 2.58$, $d_1 = 4.20$, $a_2 = 0.000389$, $b_2 = 0.00398$, $c_2 = 2.55$, and $d_2 = 2.23$.
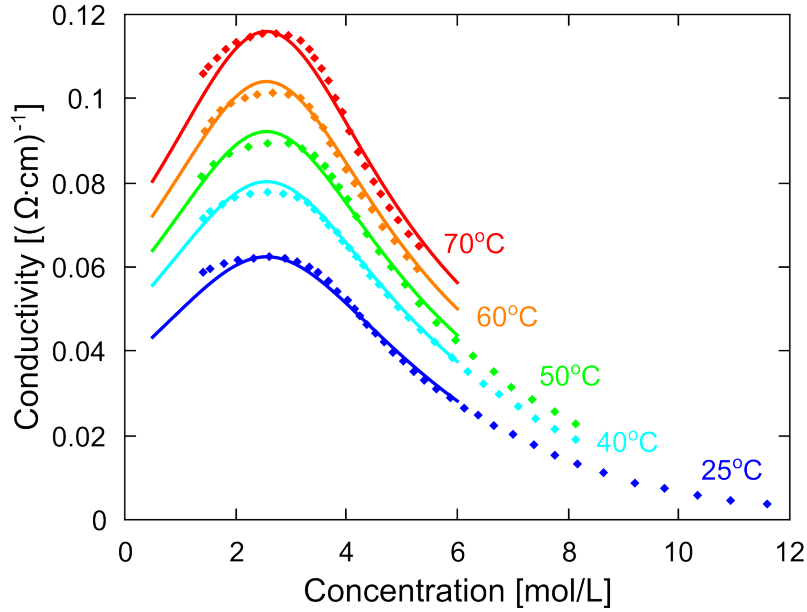

Figure 3: The conductivity of Nafion 120 vs. HCl(aq) concentration, measured by Yeo and McBreen with our fit to their data superimposed [Eq. 15] at five different temperatures.

Figure 3 shows the data from Yeo and McBreen and the fit using Equation 15. The difference between the resistive overpotential using the real conductivity data versus using the fitted curve is well below 10% for concentrations of interest at 250 $\frac{\text{mA}}{\text{cm}^2}$, or $\pm$ 5 mV in voltage terms.

The hydrogen electrode overpotential, η_H

There is an activation overpotential at the hydrogen electrode, but, because we can neglect the concentration-depletion effect due to relatively fast mass transport, we use a concentration-independent form of the Butler-Volmer equation:

$$i = i_0^H \left(\exp\left(-\alpha f \eta_H\right) - \exp\left((1-\alpha)f\eta_H\right) \right), \tag{16}$$

where i_0^H is the exchange current density at the hydrogen electrode in $\frac{\text{mA}}{\text{cm}^2}$, α is the transfer coefficient, and η_H is the activation overpotential at the hydrogen electrode in volts (14). For the model, we set the value of the transfer coefficient for both electrodes equal to 0.5.

We invert Equation 16 numerically to obtain η_H as a function of i. For a given reaction, i_0 can vary by many orders of magnitude depending on the catalyst. For example, i_0^{Cl} on flat Pt is of order 1 $\frac{\text{mA}}{\text{cm}^2}$, whereas on Ta it is of order 10^{-6} $\frac{\text{mA}}{\text{cm}^2}$. It is worth noting that Pt has been shown to have long-term stability issues in this application (7), and ruthenium dioxide based compounds are more likely to be used as a catalyst material.

One complicating factor is that the real surface area of the electrode is typically different, and sometimes vastly different, than the projected surface area of the electrode. In a PEM fuel cell, electrodes are usually made up of finely dispersed catalyst particles, which have a collective surface area much larger than the geometric area of the electrode. Technically, i_0 may also depend on temperature, but we ignore this dependence because the uncertainty in the catalytic activity and because the area multiplier is much more significant.

The exchange current density of real hydrogen electrodes has been studied in detail in the context of hydrogen-oxygen PEM fuel cells. Neyerlin *et al.* report that for a structured fuel cell electrode, the increase in the effective hydrogen exchange current density over that of a single crystal surface can be as large as a factor of 500 (15). They measured i_0^H values in the range 250-600 $\frac{mA}{cm^2}$. For the base case in this study, we set i_0^H equal to 250 $\frac{mA}{cm^2}$.

The chlorine electrode overpotential, η_{Cl}

In galvanic mode, the consumption of Cl_2 and production of Cl^- result in a depletion of Cl_2 near the electrode and an enrichment of Cl^-. The opposite occurs in electrolytic mode. For a given current density, the transport behavior of the system stabilizes at a steady-state concentration of reactant and product, so long as there exists a boundary somewhere in the system with a stable concentration and enough time is allowed to reach this steady state. In this case, we can express the concentrations of Cl_2 and Cl^- near the electrode as a function of current density.

The full, concentration-dependent Butler-Volmer equation describes the total chlorine electrode overpotential:

$$\frac{i}{i_0^{Cl}} = \frac{C_O^s(i)}{C_O^{bulk}} \exp\left(-\alpha f \eta_{Cl}\right) - \frac{C_R^s(i)}{C_R^{bulk}} \exp\left((1-\alpha) f \eta_{Cl}\right), \qquad [17]$$

where C_O^{bulk} and C_R^{bulk} are the bulk concentrations of the oxidized and reduced forms, respectively, and $C_O^s(i)$ and $C_R^s(i)$ are their respective concentrations near the electrode surface, all in $\frac{mol}{cm^3}$. The oxidized form is Cl_2 and the reduced form is Cl^-.

Measurements in our laboratory indicate that i_0^{Cl} on a flat platinum surface is about half that of hydrogen on the same surface. We are aware of no extensive study examining chlorine exchange current densities in real, structured chlorine fuel cell electrodes. Measurements from Thomassen *et al.* indicate a value for i_0^{Cl} on smooth RuO_2 of 0.01 $\frac{mA}{cm^2}$ (16). For a structured, high surface-area electrode, we expect a surface area enhancement factor (defined as the real electrode surface area over the projected electrode surface area) of about 1000 is reasonably attainable. Consequently, we assume a value of 10 $\frac{mA}{cm^2}$ for the chlorine exchange current density in the "Base Case", and later we vary this value from 1 to 1000 $\frac{mA}{cm^2}$. We expect this range to include values that will be observed in engineered (i.e. high surface area) fuel cell electrodes.

We are interested in separating the losses that arise from mass transport and those that arise from activation of the surface reaction. In order to do this, we define the mass

transport overpotential, η_{MT}, as the total chlorine overpotential (η_{Cl}, obtained from Eq. 17) minus the activation overpotential (η'_{Cl}, obtained from Eq. 16, applied to chlorine instead of hydrogen):

$$\eta_{MT} \equiv \eta_{Cl} - \eta'_{Cl} \qquad [18]$$

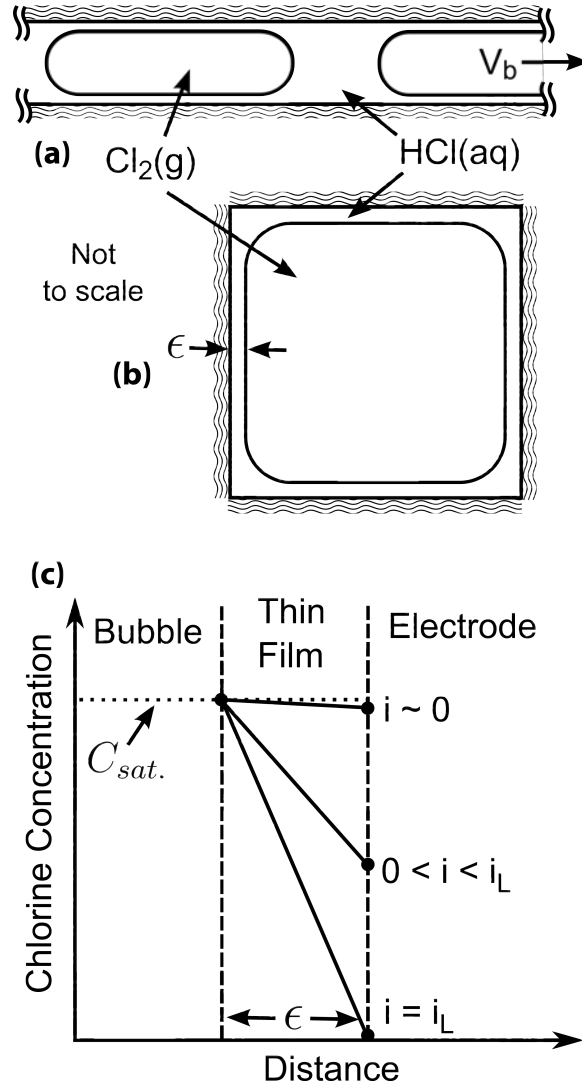The simplified mass transport picture is presented in Figure 4.

Figure 4: (a) Schematic representation of bubble-train flow in a capillary. Slugs of HCl(aq) separate bubbles of Cl_2. The thin HCl(aq) film acts as a diffusion barrier to Cl_2 reaching the electrode to react. (b) A cross-section of a square capillary exhibiting the cross-sectional bubble profile for capillary number < 0.1 (17). (c) Schematic of Cl_2 concentration versus distance from the bubble to the electrode for different current densities.

The chlorine enters and exits the cell in two-phase bubble-train flow in a square cross-section channel (Fig. 4a,b). In bubble-train flow, individual gas bubbles are interspersed between slugs of liquid. The bubbles occupy most of the cross-sectional area of the channel (Fig. 4b), but a thin film of HCl(aq) coats the channel wall and separates the gas bubble from the electrode surface. The bubbles are mostly Cl_2(g), with small amounts of HCl(g), and are surrounded by hydrochloric acid. Two-phase flow is important for the rHCFC be-

cause of the propensity of both $Cl_2(g)$ and $HCl(g)$ to dehydrate the membrane, meaning that continuous delivery of H_2O molecules to the membrane is essential. With two-phase flow, however, it is imperative that the mass transport is handled properly. If the aqueous phase sets up a diffusion barrier that is too large, the cell can become "flooded" and performance is drastically reduced. This is a problem that the low temperature hydrogen-oxygen fuel cell community has made considerable effort to overcome (18).

In order to understand mass transport through the $HCl(aq)$ thin film bubble wall, we need to know the film thickness, ε [cm], which is predictable from fluid dynamics (17,19-22). Cl_2 from inside the bubble must diffuse across this $HCl(aq)$ thin film to the electrode surface to react according to Equation 4b. As the reaction goes forward, the thin film becomes enriched in Cl^-. If the current density is sufficiently high that considerable depletion of the reactant and accumulation of the product occurs, then mass transport would limit the cell performance.

We assume that at the bubble/film boundary the concentration of Cl_2 in solution is pinned at $C_{sat.}$, which is the equilibrium concentration of $Cl_2(aq)$ dissolved in $HCl(aq)$ for the actual pressure of $Cl_2(g)$. This assumption is justified because the flux of Cl_2 toward the electrode surface is significantly smaller than the impingement rate of Cl_2 gas onto the thin film surface (alternatively, one can justify this by realizing that, since the film itself is quite thin, its surface area to volume ratio is large, meaning that $Cl_2(g)$ will be able to quickly equilibrate with the liquid film).

The diffusive flux, J $\left[\frac{mol}{cm^2 \cdot s}\right]$, is given by

$$J = -D\frac{dC}{dx} \approx -D\frac{\Delta C}{\Delta x}, \qquad [19]$$

where in the second expression we have made the quasi-stationary, linear concentration gradient approximation across the thin $HCl(aq)$ film. D is the diffusion coefficient in $\frac{cm^2}{s}$. For diffusion of Cl_2 in $HCl(aq)$, we label the diffusion coefficient D_{Cl_2}. Δx is equal to ε, the film thickness, and ΔC is the concentration difference across the thin film, namely $C_O^s(i) - C_{sat.}$ in $\frac{mol}{cm^3}$. For each mole of Cl_2 that diffuses to the electrode surface to react, $2F$ coulombs of electrons pass through the external circuit for chlorine reduction. Thus, the flux is expressed as a current density according to $i = 2FJ \cdot 1000$, where the factor of 1,000 is necessary for conversion from A to mA. Equation 19 can be solved for $C_O^s(i)$:

$$C_O^s(i) = C_{sat.} - \frac{\varepsilon}{2FD_{Cl_2}}\frac{i}{1000}. \qquad [20]$$

The film thickness ε [cm] is approximated by the following equation (16):

$$\varepsilon \approx wCa^{\frac{2}{3}}, \qquad [21]$$

where w is the width of the capillary channel and the capillary number Ca is a dimensionless number given by

$$Ca = \frac{\mu V_b}{\sigma_{surf}}. \qquad [22]$$

Here μ is the viscosity in mPa$\cdot$s, V_b is the bubble velocity in $\frac{m}{s}$, and σ_{surf} is the surface tension of HCl(aq) against Cl_2 in $\frac{mN}{m}$. In our system, we have considerable flexibility in choosing a value for ε, given that w and V_b are parameters not constrained by any other part of the system and are amenable to engineering design.

We bound values of ε by considering the relevant extremes of these parameters. We may expect V_b to vary reasonably from 0.001 to 0.1 $\frac{m}{s}$. Over the temperature and concentration range presented in work done by Laliberté, the viscosity μ varies from 0.6 to 2.4 mPa$\cdot$s (23, 24). σ_{surf} is assumed to vary similarly to the surface tension of water against air, 62-76 $\frac{mN}{m}$ over 0-80 °C (6). With these extremes, Ca varies from a minimum of 7.89×10^{-6} to a maximum of 0.00387.

A typical channel width for a fuel cell is one millimeter. We allow the channel width to vary from 0.5 to 3 mm, in which case Equation 21 yields a range on ε of 0.2 to 74 μm.

The diffusion coefficient of Cl_2 in HCl(aq) is fit to the data of Tang and Sandall (25), resulting in

$$D_{Cl_2} = 0.0392 \exp\left(\frac{-0.204}{k_B(T + 273.15)}\right), \qquad [23]$$

where k_B is Boltzmann's constant, 8.617×10^{-5} $\frac{eV}{K}$, the activation energy, -0.204, is in eV, and the prefactor is in $\frac{cm^2}{s}$. We assume D_{Cl_2} is independent of acid concentration.

We take the dependence of the saturated chlorine concentration, $C_{sat.}$ $\left[\frac{mol}{cm^3}\right]$, from the work of Hine and Inuta (26). The solubility follows Henry's law (based on the rapid impingement argument made previously), with a temperature and concentration dependent coefficient.

$$C_{sat.} = H p_{Cl_2} \cdot \frac{1}{1000 M_{Cl_2}}, \qquad [24]$$

where H is Henry's law coefficient in $\frac{g}{L\cdot atm}$, and the latter factor yields our working units of $\frac{mol}{cm^3}$ for $C_{sat.}$, with M_{Cl_2} being the molecular weight of Cl_2 of 70.9 $\frac{g}{mol}$. The concentration and temperature dependence are empirically fit by

$$H = \alpha' M_{HCl} M + \beta \qquad [25]$$

$$\log \alpha' = -1.21 \times 10^{-2} T - 1.603 \qquad [26]$$

$$\beta = 2.14 \times 10^2 T^{-1.21} \qquad [27]$$

where α' is in grams-chlorine per liter/grams-HCl per liter $\cdot$ atm, and β is in grams-chlorine per liter/atm.

We model the chloride mass transport in a similar way to the chlorine transport, with a few key differences. As Cl_2 is reduced at the electrode, Cl^- is produced and the local concentration, $C_R^s(i)$, increases. Protons also enter through the electrode at the same flux as the chloride is generated. As the concentrations increase at the electrode surface, the concentration gradient generates a diffusive flux of Cl^- and H^+ away from the electrode. We model the concentration of HCl(aq) as pinned at the bubble-thin film interface due to exchange of HCl(g) in the bubble with HCl(aq) in the thin film. The bulk solution molarity

sets the equilibrium partial pressure of HCl(g) in the bubble, which in turn maintains the thin film interface concentration at the bulk molarity. We assume the addition of new HCl(g) does not appreciably affect the partial pressure of HCl(g) in the bubble, due to the bubble's large volume with respect to the HCl(g) generated and the bubble's ability to expand longitudinally to take up any small pressure increase. The surface concentration is then modeled by:

$$C_R^s(i) = \frac{M}{1000} + \frac{\varepsilon}{FD_{HCl}} \frac{i}{1000} \qquad [28]$$

Note that the sign has changed (relative to Eq. 20) because positive fluxes of Cl$^-$ require negative current densities. Also, a factor of two is absent from the second term because there is one charge per chloride ion, as opposed to two charges per chlorine molecule in the previous case.

We fit the data of James and Gordon (27) for the diffusion coefficient of Cl$^-$ in 0.1 M hydrochloric acid to an Arrhenius function, resulting in

$$D_{Cl^-} = 0.0217 \exp\left(\frac{-0.170}{k_B(T+273.15)}\right), \qquad [29]$$

where the prefactor is in $\frac{cm^2}{s}$ and the activation energy is in eV. We assume the diffusion coefficient is independent of HCl(aq) concentration (27).

Model Results and Discussion

The model calculates the cell potential according to Equation 3, accounting for the various effects of concentration, temperature, and pressure on each of the overpotentials. We first consider the variation of the current density-voltage relationship with operating parameters for "Base Case" engineering parameters: $i_0^{Cl} = 10 \frac{mA}{cm^2}$, $\varepsilon = 3$ μm, $l = 0.178$ cm (7 mil), and $p_{Cl_2} = p_{H_2} = 1$ atm. Figure 5a shows calculated cell potentials for the Base Case EPs for three sets of OPs. The curve labeled "Standard OPs" is the cell potential at standard conditions of 25 °C and 1 M HCl.

The two most relevant performance characteristics are the cell efficiency-vs.-current-density function and the maximum cell power density. On one hand, high cell efficiency is paramount for energy storage devices because lost energy is lost revenue. It is imperative that a storage device be able to operate at high efficiencies at reasonable current densities. On the other hand, operating at higher power densities reduces the capital cost for a given power-delivery capability, because one may buy less cell area for an equivalent power. The maximum power density also permits a determination of the minimum membrane area (and associated cost) necessary to achieve a required system power. In any real storage system (used to levelize wind power, for example), the cell will operate over a distribution of current densities, constantly ramping up and down, depending of course on how much power is being generated by the turbines. Thus, both the maximum power density and the cell efficiency are important, so we explore both of these characteristics in this model.

The maximum power also serves as a convenient scalar proxy for the cell efficiency-vs.-current-density function, as the two performance characteristics are correlated, as is

apparent from Figure 5. Generally speaking, increasing the maximum power results in an efficiency increase over the entire current density range. Keep in mind, however, that the relative contributions of the individual loss mechanisms to the total loss may be significantly different at peak power than at high efficiency.

By varying the temperature and concentration using the same Base Case values for the EPs, we found the OPs that provide the performance we call "Best" and "Worst", corresponding to highest and lowest peak power density, respectively. Those curves are labeled "Best OPs" and "Worst OPs", respectively, and occur at 8 °C and 2.3 M for the "Best OPs" and 5 °C and 6 M for the "Worst OPs" (the lowest temperature and highest molarity explored in this study).

Figure 5b shows the power density as a function of current density for the same three cases. The model thus predicts more than a factor of two difference in peak power density over a modest temperature and molarity range.
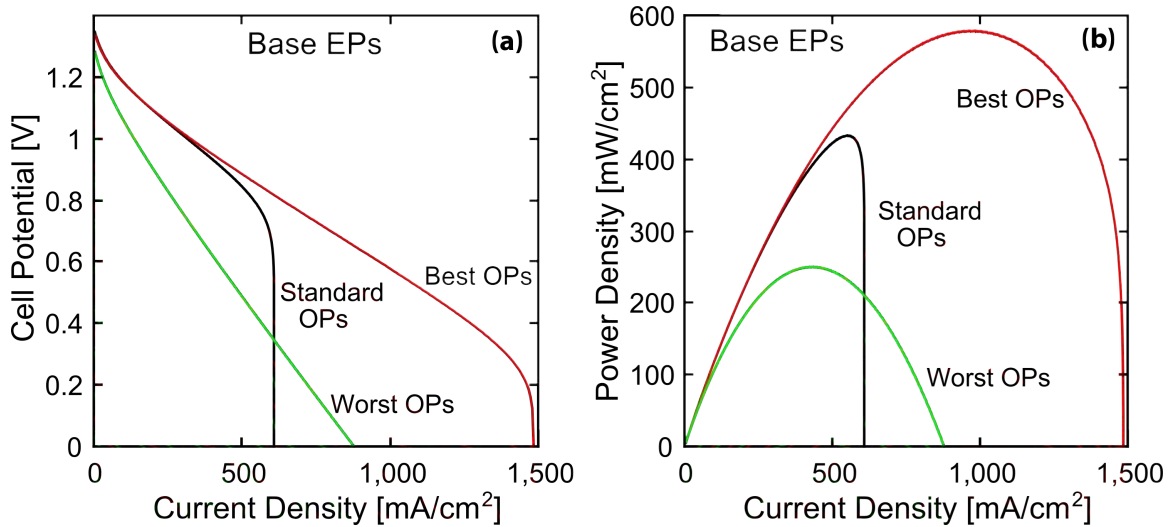
Figure 5: (a) Three different modeled cell potentials vs. galvanic current density with the same engineering parameters but different temperatures and concentrations. (b) Cell power densities for the same three cases.

For a given current density, the cell operates with a total voltage loss made up of the sum of the individual overpotentials. Figure 6a shows the current density dependence of the fractions of the total loss that each overpotential contributes for the "Best OPs" with the Base Case EPs. Figure 6b shows similar data for a so-called "More Optimal Case" that we believe represents an "approximate" practical upper-limit on the the design and operation of an rHCFC (this is discussed in more detail later in the text).

From figure 6a we see that the chlorine activation overpotential loss dominates at low current densities, remaining the most important loss until the efficiency drops to about 70%. Because energy storage devices will likely spend most of their time operating at one-way efficiencies higher than 70%, this observation makes η'_{Cl} the most important loss for a cell with this set of EPs to function as an energy storage device. η_R overtakes η'_{Cl} at about 400 $\frac{mA}{cm^2}$, and remains the most important loss at high power density until mass

17

transport kills the cell at the limiting current density of about $1500 \, \frac{\text{mA}}{\text{cm}^2}$.
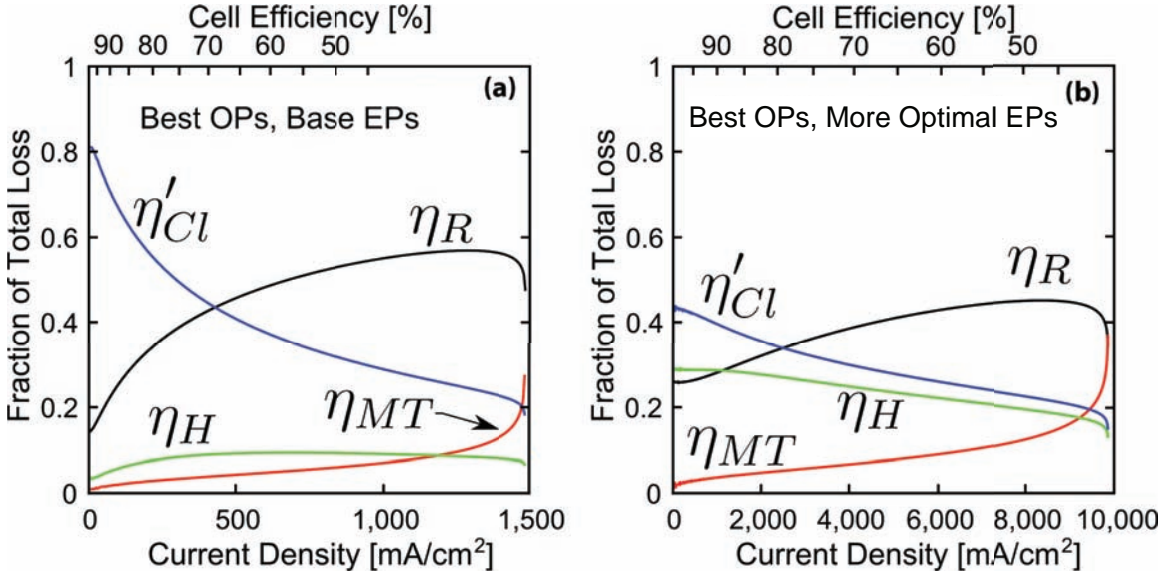

Figure 6: The four individual losses plotted as fractions of the total loss vs. galvanic current density for (a) the "Best OPs" of the Base Case; (b) the "Best OPs" of the More Optimal case. Note the different horizontal scales. The upper horizontal axis on both plots displays 5% ticks of cell efficiency.

As one may see in Figure 5b, the maximum power density can vary by more than a factor of two for different OPs for a given set of EPs. In Figure 7 we plot the dependence of cell power density on the operating conditions for two different sets of engineering parameters. The first is the set of Base Case EPs discussed previously, and the second is the aforementioned "More Optimal Case". The top row shows the maximum power density as a function of OPs, whereas the bottom row shows the power density at 90% efficiency as a function of these same OPs. Each point on these surfaces comes from a unique cell potential versus current density curve, with its own loss behavior as in Figure 5a. It is important to note that, in the "More Optimal" case, where the cell could operate at several watts per square centimeter, thermal management of the cell becomes very important. Because all of the losses experienced in the cell manifest themselves as heat, large thermal gradients could develop if the cell is not properly cooled. Fortunately, because the cell is being fueled with a two-phase liquid/gas mixture on the cathode side, the mixture itself can serve as a coolant. As long as reactant flow rates are fast enough, the relatively high heat capacity liquid phase can act as an effective coolant. This is in stark contrast to hydrogen-oxygen cells, where only gases are being delivered to the electrodes, and thus these cells often require liquid cooling through the endplates or current collectors. A more thorough treatment of heat management in rHCFCs can be found in Ref. 4.

Focusing on Figure 7a, the highest point on this surface corresponds to the "Best OPs" case discussed above. The minimum ("Worst OPs") occurs at the low temperature, high molarity corner of the domain studied. The curvature of these surfaces is determined by a competition amongst the individual losses. There are two significant effects of temperature. The increased solubility of $Cl_2(aq)$ with decreasing T, and the corresponding shift of
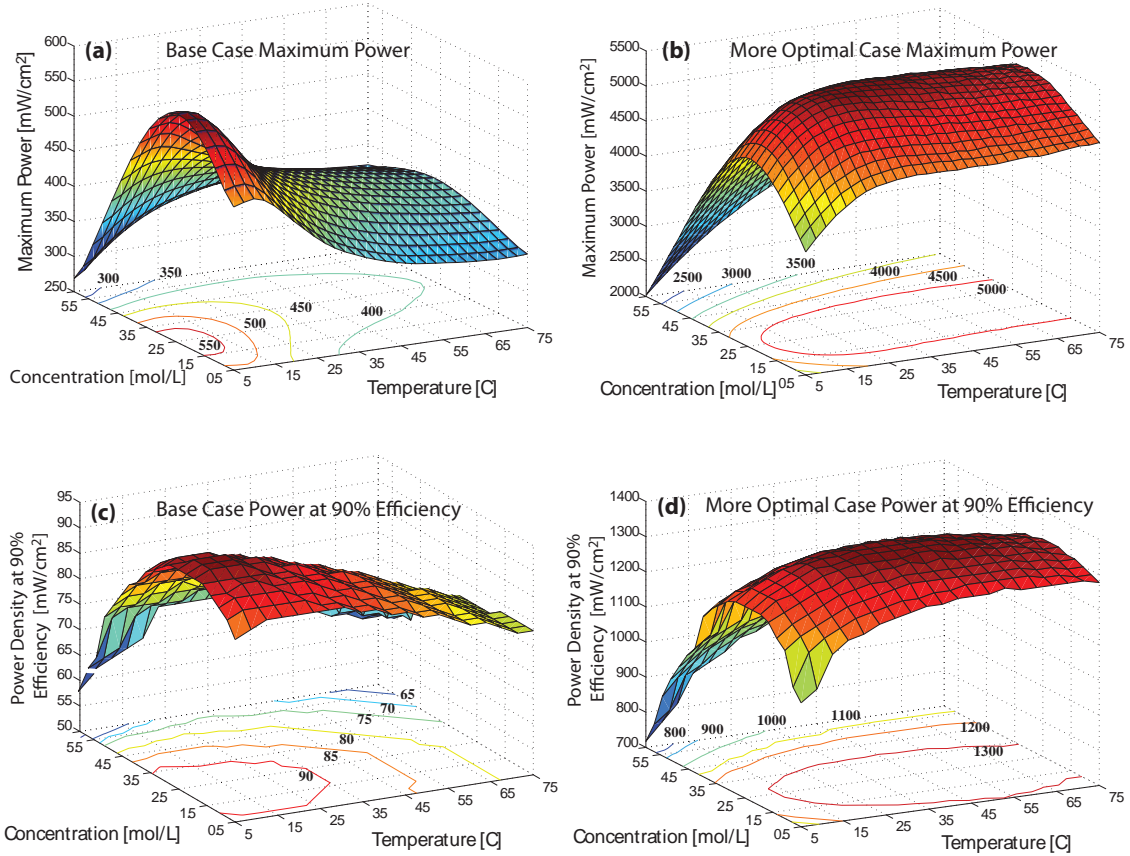
18

Figure 7: Power density vs. operating parameters. (a) Maximum power density for the cell with Base Case EPs: $i_0^{Cl} = 10 \frac{\text{mA}}{\text{cm}^2}$, $\varepsilon = 3\ \mu\text{m}$, $l = 0.178$ cm (7 mil), and atmospheric pressure. (b) Maximum power density for the cell with More Optimal Case EPs: $i_0^{Cl} = 400 \frac{\text{mA}}{\text{cm}^2}$, $\varepsilon = 1$ μm, $l = 0.025$ cm (1 mil), 5 atm gas pressures. (c) Power at 90% galvanic efficiency for the Base Case. (d) Power at 90% galvanic efficiency for the More Optimal Case. Contour lines are projected on the temperature-concentration plane. The "jaggedness" in the bottom-row plots is due to computational mesh-size limitations and is not a real effect.

the limiting current density to higher values, tends to drive the highest point toward lower T. The conductivity increase of Nafion with increasing T (see Fig. 3), as well as thermally activated electrode kinetics, tend to drive the highest point toward higher T. It is thus clear that, due to the location of the maximum at 8 °C for this set of engineering parameters, the mass transport consideration is most important for the Base Case Cell. Notice, though, that in the More Optimal Case (Figures 7b and 7d), the temperature dependence is much less significant, especially above room temperature. This is due to the lessened importance of mass transport in the More Optimal Case.

Moving back to understanding the curvature of these surfaces, there are two competing effects of changing the acid molarity. High molarity results in a lower equilibrium cell potential as well as lower Nafion conductivity. Lower equilibrium potentials correspond to lower efficiency in general, because the individual energy losses make up a larger fraction of total chemical energy converted. As the molarity decreases, the equilibrium cell po-

tential starts to increase, as does the Nafion conductivity. The conductivity of the Nafion peaks at about 2.5 M and then starts to fall off again with decreasing molarity, whereas E_{eq} continues to rise. The competition between these two effects after the peak Nafion conductivity results in a maximum at about 2.3 M.

It is also important to note that the maximum power surfaces and the surfaces representing the power density at 90% efficiency are roughly the same shape for both the Base Case cell and the More Optimal case cell. This intuitively makes sense: operating conditions that permit high-efficiency operation will also provide the highest possible maximum power densities.

In Figure 8, we report the variation of the maximum peak power (the height of the highest point in Figure 7) as each of the engineering parameters (other than the hydrogen exchange current density, which is fixed at $i_0^H = 250 \; \frac{\text{mA}}{\text{cm}^2}$) is varied away from the Base Case while keeping the other four EPs fixed. For each set of EPs a surface similar to that in Figure 7 is generated, and the "Best OPs" and "Worst OPs" for that set of EPs are recorded in Figure 8. The latter are included as an indication of the performance sensitivity to OPs.

In Figure 8a we varied i_0^{Cl} from the certainly attainable value of 1 $\frac{\text{mA}}{\text{cm}^2}$, to the likely unattainable value of 1000 $\frac{\text{mA}}{\text{cm}^2}$. For this set of EPs there are significantly diminishing returns for efforts to increase i_0^{Cl} beyond the Base Case, but decreasing i_0^{Cl} below the Base Case causes a degradation in performance.

In Figure 8b we show how performance rapidly increases with decreasing membrane thickness, due to decreasing membrane resistance. Nafion is currently commercially available in thicknesses from 25 to 250 μm, but engineering a fuel cell with the thinnest membrane can be difficult, as it serves as the only separator between two highly reactive gases. As we refer back to Figure 6, we see that, in the absence of significant mass transport loss, the resistance overpotential dominates the other overpotentials at high current densities, including current densities at which the maximum power densities are located.

In Figure 8c we show that the power performance declines considerably for large values of the acid layer thickness ε; this occurs because of small limiting current densities. As ε is decreased, the gain in power is roughly linear until a rapid upturn at about 2 μm. This results from a trade-off between mass transport and resistance loss. For $\varepsilon > 2 \; \mu$m, mass transport loss dominates the temperature sensitivity; hence the optimal operating temperature is driven down for increased Cl_2 solubility. As ε drops below 2 μm, the mass transport loss has become small enough that higher cell temperatures are selected to lower the membrane resistance. When $\varepsilon = 0.5 \; \mu$m, the optimal temperature has increased to 67.5 °C, where the membrane conductivity is significantly higher over the entire molarity range. We thus see that, as mass transport is effectively made less important by decreasing the size of ε, the optimal temperature for cell operation increases.

In Figure 8d we show how the cell performance depends on the pressure of H_2 and Cl_2 gases (we always maintain $p_{Cl_2} = p_{H_2}$). Higher pressure gives a modest boost to the open circuit potential. However, this effect is dominated by a covariant conductivity increase in the PEM. Increasing the pressure raises the solubility of $Cl_2(g)$ proportionally, which decreases the need to go to low temperature for solubility enhancement, thereby allowing
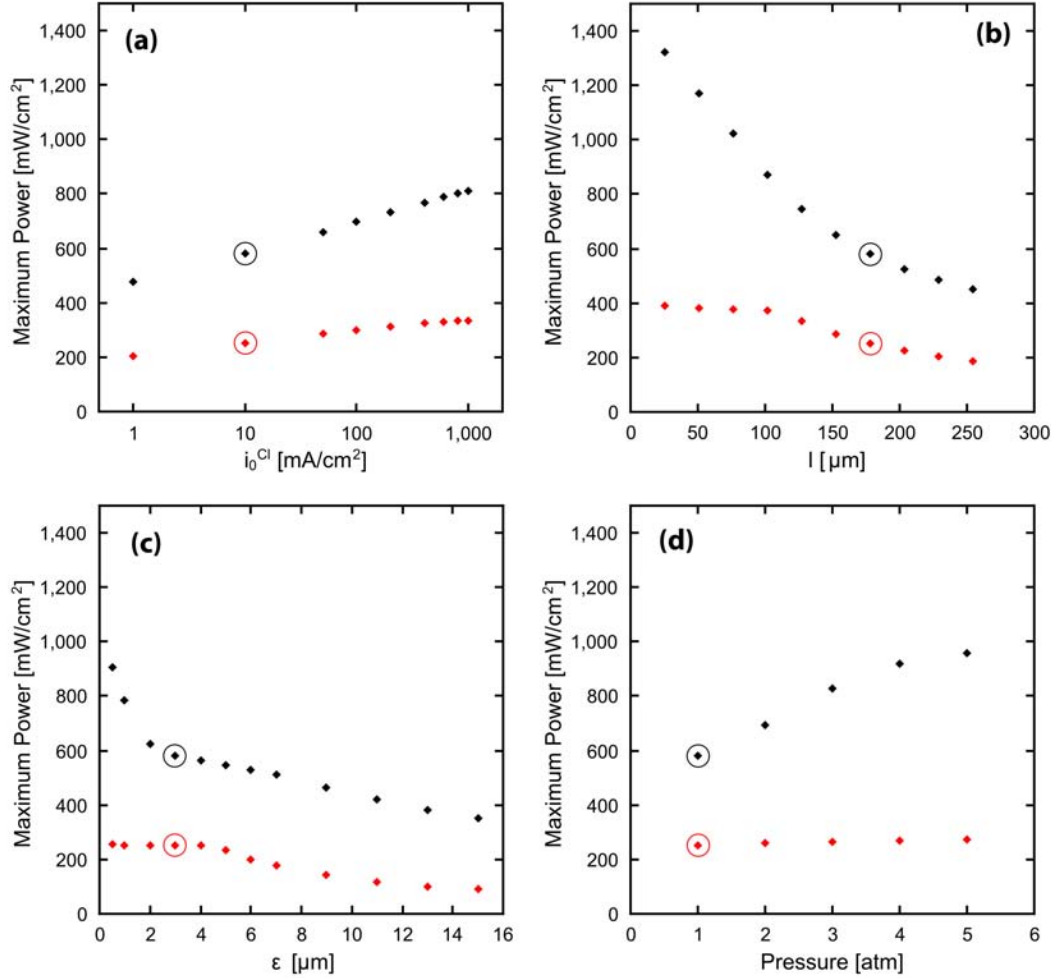
Figure 8: Dependence of performance on deviation from Base Case engineering parameters. Maximum power densities are displayed as a function of each engineering parameter with the others held at the Base EP values: $i_0^H = 250 \frac{\text{mA}}{\text{cm}^2}$, $i_0^{Cl} = 10 \frac{\text{mA}}{\text{cm}^2}$, $\varepsilon = 3$ μm, and $l = 0.178$ cm (7 mil). (a) Chlorine exchange current density, i_0^{Cl}. (b) Nafion membrane thickness, l. (c) Bubble thin film thickness, ε. (d) The cell pressure, $p_{Cl_2} = p_{H_2}$. Base case is circled. The black (upper) dots represent the "Best OPs" for a given set of EPs, while the red (lower) dots represent the "Worst OPs" for the same set of EPs.

an increase in temperature for better Nafion conductivity. The optimal temperature starts at 8 °C at 1 atm, and increases steadily until it reaches 68 °C at 5 atm.

The average "Best OP" molarity over the EP space studied in Figure 8 is 2.3 M with a standard deviation of 0.2 M. This suggests that the most dominant concentration effect is the membrane conductivity, which peaks at around 2.5 M for all temperatures (Fig. 3).

While Figure 8 focuses on the effects of varying the individual engineering parameters on the maximum power density, it is also important to understand how varying the EPs would affect the cell power density at high efficiency. From Figure 6a, it is clear that the dominant loss at 90% galvanic efficiency is the chlorine activation overpotential. Thus,

varying the chlorine electrode exchange current density should have the largest effect on cell performance at 90% efficiency. Figure 9a confirms this expectation. Figure 9b shows that the Nafion thickness is somewhat important to cells operating at high efficiencies. This is consistent with Figure 6a, which shows the resistive overpotential through the membrane as the second most important loss at 90% efficiency. Notice from Figures 9c and 9d that cell performance at 90% efficiency is only very slightly dependent on gas pressures or diffusion layer thickness: this is due to the unimportance of mass transport at low current densities.
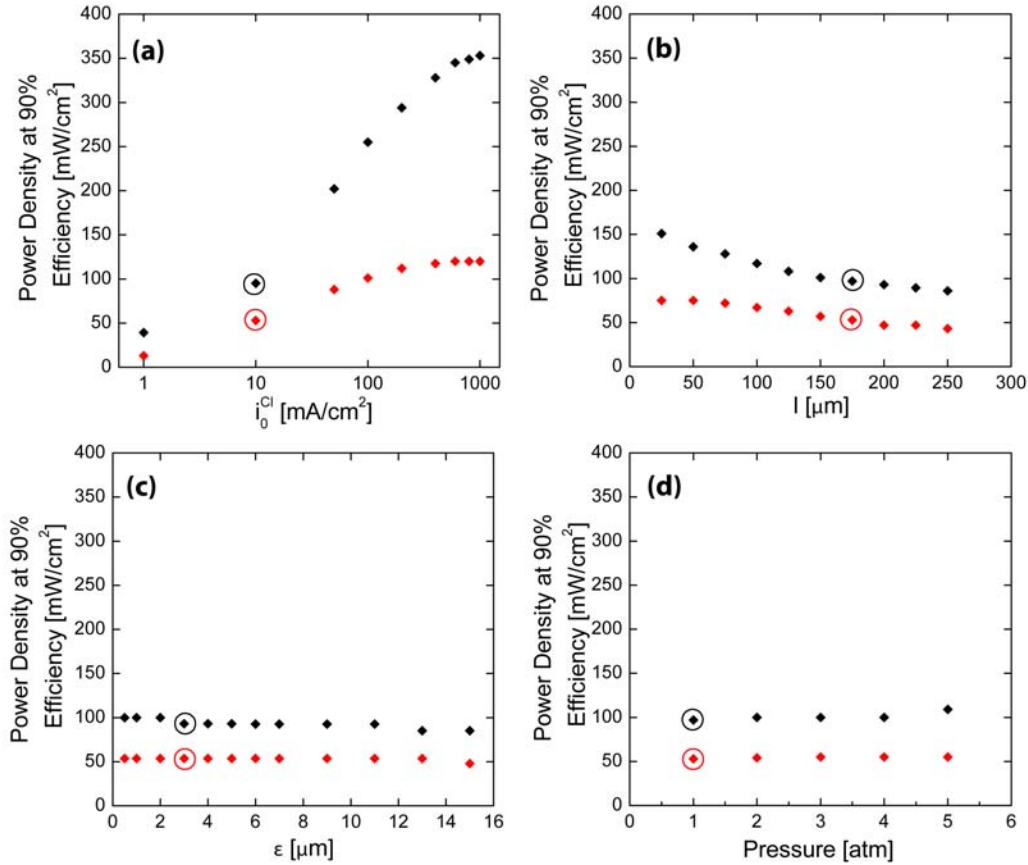
Figure 9: Dependence of power density at 90% galvanic efficiency on deviation from Base Case engineering parameters. Power densities are displayed as a function of each engineering parameter with the others held at the Base EP values: $i_0^H = 250 \frac{\text{mA}}{\text{cm}^2}$, $i_0^{Cl} = 10 \frac{\text{mA}}{\text{cm}^2}$, $\varepsilon = 3$ μm, and $l = 0.178$ cm (7 mil). (a) Chlorine exchange current density, i_0^{Cl}. (b) Nafion membrane thickness, l. (c) Bubble thin film thickness, ε. (d) The cell pressure, $p_{Cl_2} = p_{H_2}$. Base case is circled. The black (upper) dots represent the "Best OPs" for a given set of EPs, while the red (lower) dots represent the "Worst OPs" for the same set of EPs.

It is interesting to use the model to predict the absolute best performance one might expect from an rHCFC because it provides a target for an experimental R&D program. We input so-called "More Optimal" values of all of the parameters – the best values of the EPs that we believe are plausibly attainable with further R&D – and calculated the ideal operating conditions for these EPs. For the More Optimal EPs, we set $i_0^H = 600$

$\frac{mA}{cm^2}$, a value which has already been obtained for the hydrogen electrode in a hydrogen-oxygen fuel cell (12). In light of preliminary indications of fast chlorine kinetics in our laboratory, we assume that the chlorine catalysis will be able to almost catch up to the value for hydrogen in the future, and we set $i_0^{Cl} = 400 \frac{mA}{cm^2}$. The thinnest Nafion membrane that we expect could be employed is about 25 μm, and we set l to this value. We chose a relatively insignificant, but physically obtainable, value of ε at 1 μm. Finally, we set the gas pressures to 5 atm, which approaches chlorine's vapor pressure of approximately 5.8 atm at standard temperature. The resultant "Best OPs" maximum power from the More Optimal EPs was 5460 $\frac{mW}{cm^2}$, which occurred at 28 $^\circ$C and 2.4 M (see Fig. 10).
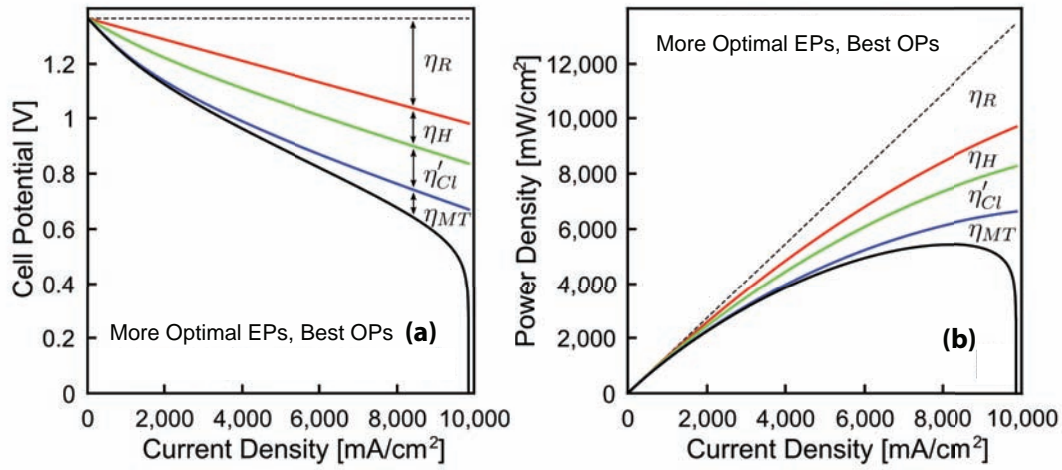

Figure 10: Performance for the "Best OPs" of the More Optimal Case EPs. Dotted lines represent thermodynamic limit and solid black curves represent performance accounting for all four loss mechanisms. (a) Cell potential vs. current density; note that the horizontal scale extends to very large current densities. The arrows identify individual losses from each of the four mechanisms. (b) Galvanic power density corresponding to potentials in (a).

Figure 11 shows the cell efficiency versus power density for Base Case EPs and More Optimal Case EPs (both under "Best OP" conditions). The "Best OP" maximum power density for the Base Case EPs was 579 $\frac{mW}{cm^2}$, which can be seen in the figure.

The curve labeled "More Optimal" is the upper-bound-on-performance case outlined above. The cell efficiency is remarkably higher in both directions, exceeding 90% one-way at a galvanic power density of about 1150 $\frac{mW}{cm^2}$, and exceeding 90% one-way at an electrolytic power density of about 1650 $\frac{mW}{cm^2}$. Attaining even half of this performance would result in a highly efficient storage system with much smaller total cell area, and thus lower costs, than the Base Case. In contrast, the Base Case EPs can reach 90% galvanic efficiency at a power density of only about 100 $\frac{mW}{cm^2}$ and 90% electrolytic efficiency at about the same current density.

Figure 6b shows that no individual loss completely overwhelms all of the others in the More Optimal case. Both η_{Cl}' and η_H make up a larger portion of the loss than η_R at
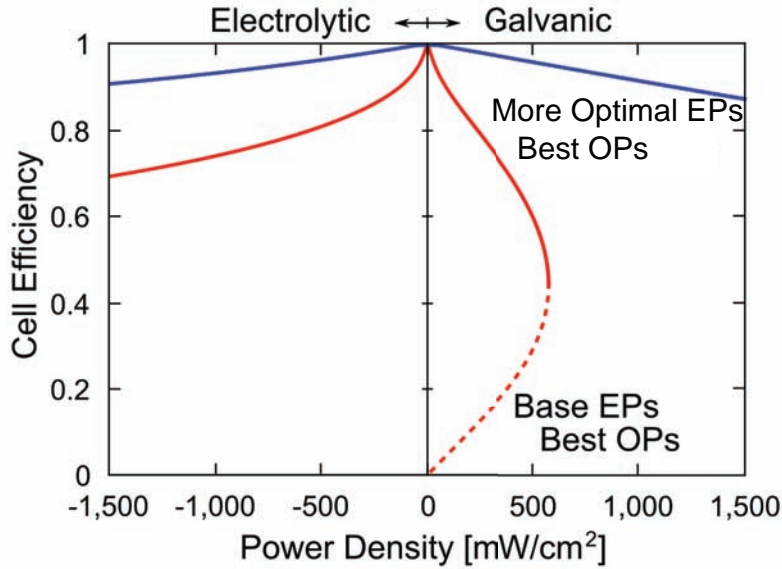
Figure 11: Cell efficiency as a function of power density for the Base Case EPs and More Optimal Case EPs, both at "Best OPs". The transition to a dashed line on the Base Case curve highlights an undesirable region of operation, as the efficiency decreases with decreasing power density.

current densities leading to efficiencies exceeding 90%. With increasing current density, η_R eventually overtakes both of the activation losses, and becomes the dominant loss for an extended portion of the current density range. Finally, η_{MT} kills the cell at the limiting current density of about 10 $\frac{A}{cm^2}$.

It is interesting to gauge the importance of the individual engineering parameters as we back them off of their More Optimal values. Decreasing i_0^{Cl} by 25% brings the maximum power down from 5460 $\frac{mW}{cm^2}$ to 5340 $\frac{mW}{cm^2}$. Decreasing i_0^H by 25% has the same effect. Increasing l by 25% takes the maximum power down to 4980 $\frac{mW}{cm^2}$. Increasing ε by 25% takes the maximum power down to 5100 $\frac{mW}{cm^2}$. Finally, the most significant performance reduction came from decreasing the gas pressure by 25%, which brings the maximum power to 4700 $\frac{mW}{cm^2}$. None of these individual shortcomings would render the cell performance unacceptable.

Summary

We have developed a simple model of an rHCFC for a configuration in which the chlorine electrode is exposed to bubble-train flow of reactant $Cl_2(g)$ and product $HCl(aq)$. The model analyzes the expected losses from Nafion ohmic loss, $Cl_2(aq)$ mass transport through the bubble wall, chlorine activation, and hydrogen activation.

We considered the effects of five cell engineering parameters: hydrogen exchange current density, chlorine exchange current density, gas pressure, membrane thickness, and

bubble wall thickness. The model predicted the cell potential vs. current density in both galvanic and electrolytic directions. For each set of EPs, we varied the OPs over a range where the model approximations hold, and identified the Best OPs for each set of EPs.

We started with "Base Case EPs", which we believe are technically feasible today: i_0^{Cl} = 10 $\frac{mA}{cm^2}$; ε = 3 μm; l = 0.178 cm (7 mil); and atmospheric pressure. We showed the contributions to the total loss vs. current density for each of the four loss mechanisms. Chlorine activation overpotential is the largest loss mechanism for low current densities ($i < 400\frac{mA}{cm^2}$, $\eta > 0.7$), whereas for higher current densities the ohmic loss in the Nafion dominates the losses.

We varied each EP (except for i_0^H) systematically while holding all the other EPs at their "Base Case" values, found the best and worst OPs for each set of EPs, and report, for the best OPs for each set of EPs, the maximum power density and the power density at 90% galvanic efficiency. Particularly important to improving high-efficiency operation is increasing the chlorine exchange current density, either by improving chlorine catalysis or by increasing the specific surface area of the chlorine electrode. Particularly important to achieving high maximum power densities is to safely use as thin of a membrane as possible. Assuming mass transport is kept insignificant by proper management of the diffusion layer thickness, or by operating the cell at high pressures, then gains in mass transport will not significantly affect operation at peak power or high efficiency.

We identified a set of "More Optimal EPs" representing ambitious targets that we believe to be attainable with further R&D: i_0^{Cl} = 400 $\frac{mA}{cm^2}$; ε = 1 μm; l = 25 μm (1 mil); and 5 atm pressure. This case provides a reasonable estimate of the upper bound on the performance of a hydrogen-chlorine fuel cell of this type: a cell efficiency exceeding 90% one-way at a galvanic power density of about 1150 $\frac{mW}{cm^2}$ and at an electrolytic power density of about 1650 $\frac{mW}{cm^2}$. The maximum power density of such a cell would be about 5400 $\frac{mW}{cm^2}$. Although these are ambitious figures, we believe that if the performance of a real system were to approach even half of these values, regenerative hydrogen chlorine fuel cells could become economically viable electricity storage devices.

Acknowledgments

References

1. J. M. Eyer, J. J. Iannucci and G. P. Corey, Energy Storage Benefits and Market Analysis Handbook, A Study for the DOE Energy Storage Systems Program, in Sandia National Labratories (2004).

2. E. N. Balko and J. F. McElroy, in *Power Sources Conference*, 29th, Atlantic City, NJ, June 9-12, 1980, Proceedings. (A81-49478 24-44) (1980).

3. E. B. Anderson, E. J. Taylor, G. Wilemski and A. Gelb, *J. Power Sources*, **47**, 321 (1994).

4. D. T. Chin, R. S. Yeo, J. McBreen and S. Srinivasan, *J. Electrochem. Soc.*, **126**, 713 (1979).

5. L. J. Nuttall, J. F. McElroy, S. Srinivasan and T. G. Hart, in *Alternative energy sources; Proceedings of the Miami International Conference*, Miami Beach, Fla., December 5-7, 1977. Volume 8. (A79-34106 13-44) (1977).

6. R.S. Yeo, J. McBreen, A.C.C. Tseung, and S. Srinivasan, *J. Appl. Electrochem.*, **10**, 393 (1979).

7. M. Thomassen, B. Borresen, G. Hagen, and R. Tunold, *J. Appl. Electrochem.*, **33**, 9 (2003).

8. D.J. Eames and J. Newman, *J. Electrochem. Soc.*, **142**, 3619 (1995).

9. M. Thomassen, B. Borresen, K. Scott, and R. Tunold, *J. Power Sources*, **157**, 271 (2006).

10. D. R. Lide, *CRC Handbook of Chemistry and Physics*, 88th Edition (CRC Handbook of Chemistry and Physics), CRC (2007).

11. J. I. Partanen, P. M. Juusola, K. P. Vahteristo and A. J. G. de Mendonca, *J. Solution Chem.*, **36**, 39 (2007).

12. P. Novotný and O. Söhnel, *J. Chem. Eng. Data*, **33**, 49 (1988).

13. R. S. Yeo and J. McBreen, *J. Electrochem. Soc.*, **126**, 1682 (1979).

14. A. J. Bard and L. R. Faulkner, *Electrochemical Methods: Fundamentals and Applications*, p. 87, Wiley (2000).

15. K. C. Neyerlin, W. Gu, J. Jorne and H. A. Gasteiger, *J. Electrochem. Soc.*, **154**, B631 (2007).

16. M. Thomassen, B. Borresen, G. Hagen and R. Tunold, *Electrochimica Acta*, **50**, 1157 (2005).

17. W. B. Kolb and R. L. Cerro, *Phys. Fluids A*, **5**, 1549 (1993).

18. R. Anderson, L. Zhang, Y. Ding, M. Blanco, X. Bi and D. P. Wilkinsons, *J. Power Sources*, **195**, 4531 (2010).

19. L. W. Schwartz, H. M. Princen and A. D. Kiss, *J. Fluid Mechanics*, **172**, 259 (1986).

20. T. C. Thulasidas, M. A. Abraham and R. L. Cerro, *Chem. Eng. Sci.*, **50**, 183 (1995).

21. H. Wong, C. J. Radke and S. Morris, *J. Fluid Mechanics*, **292**, 71 (1995).

22. M. Muradoglu and H. A. Stone, *J. Fluid Mechanics*, **570**, 455 (2007).

23. M. Laliberté, *J. Chem. Eng. Data*, **52**, 321 (2007).

24. M. Laliberté, *J. Chem. Eng. Data*, **52**, 1507 (2007).

25. A. Tang and O. Sandall, *J. Chem. Eng. Data*, **30**, 189 (1985).

26. F. Hine and S. Inuta, *Bull. Chem. Soc. Jpn.*, **41**, 71 (1968).

27. W. A. James and A. R. Gordon, *J. Chem. Phys.*, **7**, 963 (1939).